Pressure-tunable large anomalous Hall effect of the ferromagnetic kagome-lattice Weyl semimetal Co_{3}Sn_{2}S_{2}

Xuliang Chen, Maoyuan Wang, Chuanchuan Gu, Shuyang Wang, Yonghui Zhou, Chao An, Ying Zhou, Bowen Zhang, Chunhua Chen, Yifang Yuan, Mengyao Qi, Lili Zhang, Haidong Zhou, Jianhui Zhou, Yugui Yao, and Zhaorong Yang

Phys. Rev. B **100**, 165145 — Published 30 October 2019

DOI: 10.1103/PhysRevB.100.165145

Pressure-tunable large anomalous Hall effect of the ferromagnetic kagome-lattice Weyl semimetal $Co_3Sn_2S_2$

Xuliang Chen,[1,*] Maoyuan Wang,[2,*] Chuanchuan Gu,[3,4] Shuyang Wang,[1,4] Yonghui Zhou,[1] Chao An,[5] Ying Zhou,[1] Bowen Zhang,[1,4] Chunhua Chen,[1,4] Yifang Yuan,[1,4] Mengyao Qi,[5] Lili Zhang,[6,7] Haidong Zhou,[8,9] Jianhui Zhou,[1,†] Yugui Yao,[2,‡] and Zhaorong Yang[1,5,10,§]

[1] *Anhui Province Key Laboratory of Condensed Matter Physics at Extreme Conditions, High Magnetic Field Laboratory, Chinese Academy of Sciences, Hefei 230031, China*
[2] *Key Laboratory of advanced optoelectronic quantum architecture and measurement (MOE), Beijing Key Laboratory of Nanophotonics and Ultrafine Optoelectronic Systems, School of Physics, Beijing Institute of Technology, Beijing 100081, China*
[3] *Department of Materials Science and Engineering, Southern University of Science and Technology, Shenzhen 518055, China*
[4] *School of Physical Sciences, University of Science and Technology of China, Hefei 230026, China*
[5] *Institutes of Physical Science and Information Technology, Anhui University, Hefei 230601, China*
[6] *Shanghai Institute of Applied Physics, Chinese Academy of Sciences, Shanghai 201204, China*
[7] *Shanghai Synchrotron Radiation Facility, Shanghai Advanced Research Institute, Chinese Academy of Sciences, Shanghai 201204, China*
[8] *Department of Physics and Astronomy, University of Tennessee, Knoxville, Tennessee 37996-1200, USA*
[9] *Key laboratory of Artificial Structures and Quantum Control (Ministry of Education), School of Physics and Astronomy, Shanghai JiaoTong University, Shanghai 200240, China*
[10] *Collaborative Innovation Center of Advanced Microstructures, Nanjing, 210093, China*

(Dated: October 17, 2019)

We report a systematic high-pressure study of magnetic topological semimetal $Co_3Sn_2S_2$ through measurements of synchrotron x-ray diffraction (XRD), magnetization, electrical and Hall transports combined with first-principle theoretical calculations. No evident trace of structural phase transition is detected through synchrotron x-ray diffraction over the measured pressure range of 0.2-50.9 GPa. We find that the ferromagnetism and the anomalous Hall resistivity are monotonically suppressed as increasing pressure and almost vanish around 22 GPa. The anomalous Hall conductivity varies non-monotonically against pressure at low temperatures, involving competition between original and emergent Weyl nodes. Combined with first-principle calculations, we reveal that the intrinsic mechanism due to the Berry curvature dominates the anomalous Hall effect under high pressure.

I. INTRODUCTION

Topological semimetals possess a nontrivial band topology in momentum space, leading to many novel properties such as chiral magnetic effect, ultrahigh mobility, negative longitudinal magnetoresistance and three-dimensional quantum Hall effect.[1–5] Recently, nonmagnetic topological semimetals have been predicted in a large amount of crystals through first-principle calculations,[6–8] some of which have been confirmed experimentally. However, realistic intrinsic magnetic topological semimetals are extremely rare. The entanglement between magnetism and nontrivial topology could further enrich the physical properties of quantum states, resulting in exotic transport phenomena such as large anomalous Hall effect (AHE).[9–11] The AHE, usually driven by the spontaneous magnetization rather than an external magnetic field, not only deepens the understanding of topology and geometry of Bloch electrons in crystals without time reversal symmetry[12,13] but also inspires potential applications of quantum materials in next generation electronics.[14,15]

Very recently, a series of experiments suggest that Shandite-type compound $Co_3Sn_2S_2$ can be a magnetic Weyl semimetal and shows a giant anomalous Hall conductivity (AHC).[16,17] $Co_3Sn_2S_2$ consists of Co_3Sn layers sandwiched by sulfur atoms. It is known as a half-metallic ferromagnet, whose magnetism originates from the magnetic cobalt atoms on a kagome lattice in the *a*-*b* plane with the spontaneous polarization along the *c* axis.[18–20] The interplay between this out-of-plane magnetization and the nontrivial topology of the Bloch bands accounts for the novel electromagnetic responses.[16,17,21–26]

Pressure has proven to be an effective and clean means to tune the lattice and electron degrees of freedom in topological materials. There have been several reports on pressure tuning of anomalous transports like in dilute magnetic semiconductor (In, Mn)Sb[27–29] and MnSi.[30] For magnetic topological semimetals, such as $Co_3Sn_2S_2$, the studies on how high pressure modifies the anomalous Hall transports are still lack. In addition, unlike the conventional element substitution method for investigating mechanisms of the AHE, high pressure does not inject extra impurities into the material and could well reveal its intrinsic properties and mechanisms of the AHE.

In this work, we systematically investigate the pressure effect on the AHE in magnetic Weyl semimetal $Co_3Sn_2S_2$ through multiple experimental measurements and first principle calculations. The structure of $Co_3Sn_2S_2$ is sta-

ble up to 50.9 GPa. The ferromagnetism and the anomalous Hall resistivity are greatly suppressed as pressure increases and vanish simultaneously around 22 GPa. The AHC shows a non-monotonic change with pressure in the low temperature region, which can be captured by theoretical calculations in terms of competing evolutions of original and emergent Weyl nodes.

II. MATERIALS AND METHODS

The preliminary synthesized polycrystalline $Co_3Sn_2S_2$ was prepared by standard solid state reaction method from high purity elements (Alfa Aesar). Single crystals of $Co_3Sn_2S_2$ were grown by flux-growth technique with Sn as the flux. The crude materials with a molar ratio of $Co_3Sn_2S_2$:Sn of 1:8.5 were sealed in an evacuated quartz tube. The mixture was then heated to 850 °C followed by a slow cooling down to 700 °C. Excessive flux Sn on the crystal surface was removed by high-temperature centrifuging. Finally, plate-like single crystals with perfect hexagonal geometry can be obtained. The structure of $Co_3Sn_2S_2$ was characterized by single crystal and powdered x-ray diffraction at room temperature. The transport properties were measured by using an in-lab multifunctional physical properties measurement system. The basic magnetism of single crystal $Co_3Sn_2S_2$ was checked by using SQUID-VSM-7T (Quantum Design, MPMS3). The characterization results (see Appendix A) are in good accordance with previous reports.[16,17]

In situ high pressure synchrotron x-ray diffraction (XRD) experiments were carried out at room temperature at the beam line BL15U1 of the Shanghai Synchrotron Radiation Facility (SSRF) (λ=0.6199 Å). The DIOPTAS program was used for image integrations. Standard Rietveld refinement procedure was used to fit the XRD patterns by using the RIETICA program with the Le Bail method. Daphne 7373 was used as the pressure transmitting medium. Ruby fluorescence method was used to determine the pressure at room temperature.

The DC magnetization (M) measurement at high pressures was carried out by using a Be-Cu alloy diamond anvil cell designed by the Honest Machinery Designer (HMD) Corporation, Japan on the SQUID-VSM-7T (Quantum Design, MPMS3). The diamond culet is 800 μm. A Be-Cu alloy gasket was pre-indented to a thickness of ∼90 μm and a central hole of ∼550 μm was then drilled by laser ablation as sample chamber. A piece of single crystal $Co_3Sn_2S_2$ with a dimension of about 480 × 480 × 80 μm was loaded into the sample chamber without pressure medium. A ruby ball of ∼5 μm locating on the surface of the sample was used as a pressure manometer. Ruby fluorescence method was used to determine the pressure at room temperature. As the sample size is very small (∼80 × 480 × 80 μm) and the DAC background signal is relatively strong, we first cooled the sample under a magnetic field of 3000 Oe and then measured the magnetization at 100 Oe in the heating process.

In transport measurements, high pressure was generated by a Be-Cu alloy diamond anvil cell made by the Honest Machinery Designer (HMD) Corporation, Japan. The diameter of the diamond culet is 300 μm. A freshly cleaved single-crystal piece of ∼120 × 70 × 10 μm (its exact lattice orientation is undetermined) was loaded with NaCl powder as the pressure transmitting medium. Ruby fluorescence method was used to determine the pressure at room temperature. A five-probe (four-probe) method was employed to perform the temperature dependent Hall resistivity (ρ_H) [longitudinal resistivity (ρ_{xx})] measurement in an in-lab multifunctional physical properties measurement system (1.8-300 K; ±9 T). The Hall resistivity ρ_H was calculated via $\rho_H = t \cdot V_{yx}/I_x$, with t the thickness of the sample (10 μm), V_{yx} the transverse Hall voltage and I_x the longitudinal current applied within the xy axis (in-plane). To strip the possible contribution from the longitudinal magnetoresistance due to non-perfect balance of the voltage drop V_{yx} at zero z-axis (out-of-plane) field (B_z), ρ_H is anti-symmetrized through $[\rho_H = (\rho_H(B_z) - \rho_H(-B_z))/2]$.

First principles calculations are performed by using Vienna ab initio simulation package (VASP)[31] based on the density function theory with Perdew-Burke-Ernzerhof (PBE) parameterization of generalized gradient approximation (GGA).[32,33] The energy cutoff of the plane wave basis is set as 300 eV, and the Brillouin zone of $Co_3Sn_2S_2$ is sampled by 8 × 8 × 8 k-mesh. The ionic positions are fully optimized until the force on each atom was less than 0.01 eV/Å while the lattice parameters are fixed as the experimental value. The intrinsic anomalous Hall conductivity is calculated based on the wannier90 code[34,35] with s, p, d orbitals of Co atoms and s, p orbitals of S and Sn atoms. The k-mesh for intrinsic hall conductivity calculation is 100 × 100 × 100 with an adaptive refinement mesh of size of 5 × 5 × 5.

III. X-RAY DIFFRACTION UNDER PRESSURE

Our high-pressure XRD data shows that the structure of $Co_3Sn_2S_2$ is stable with pressures up to 50.9 GPa. In Fig. 1(a), XRD peaks at all pressures can be well indexed by the Shandite-type structure with space-group $R\bar{3}m$ (No. 166) and no secondary phase is detected. In total, six parameters have been refined: scale factor, three peak width parameters (U, V, W) and lattice parameters (a and c), respectively. Two representative refinement profiles are shown in Figs. 1(b) and (c). The structural parameters a, c and c/a extracted from the standard Rietveld refinement vary smoothly with pressure and show no anomaly [Figs. 1(d)-(f)]. Figure 1(g) shows the unit cell volume as a function of pressure, which is fitted by the third-order Birch-Murnaghan formula.[36] The fitting yields the volume at zero plressure V_0=327.7 (±0.6) Å^3, the bulk modulus B_0=136.0 (±4.7) GPa and its first-order derivative $B_0^{'}$=3.6 (±0.2).

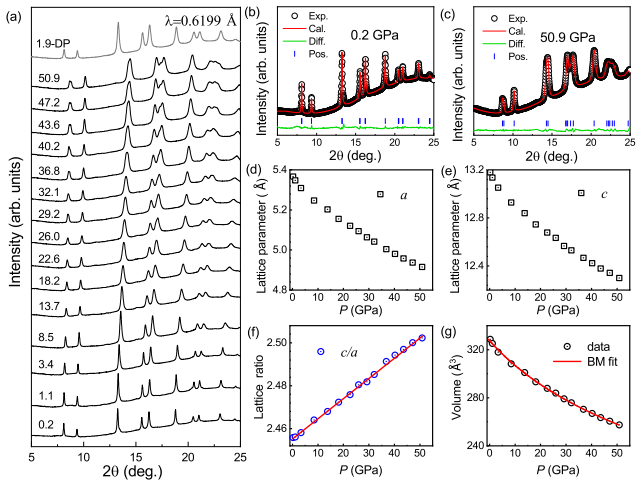

FIG. 1. (a) Synchrotron XRD patterns of $Co_3Sn_2S_2$ at various pressures up to 50.9 GPa (λ=0.6199 Å). (b,c) Fits of the XRD patterns at 0.2 and 50.9 GPa. (d,e) Evolutions of lattice parameters versus pressure. (f) Ratio of lattice parameters c/a as a function of pressure. The red line is a linear fit to the data. (g) The unit-cell volume versus pressure. The data (black circle) is fitted by the third-order Birch-Murnaghan formula (red line).

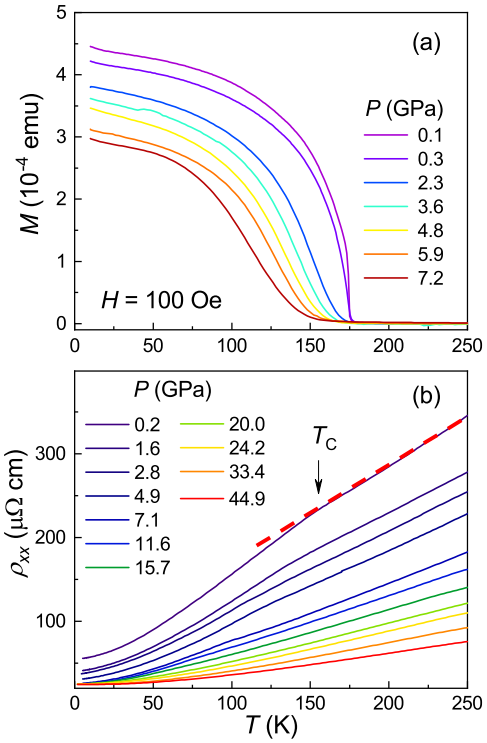

FIG. 2. (a) Temperature dependence of magnetization M under different pressures to 7.2 GPa with an applied magnetic field of 100 Oe. (b) Temperature dependence of electric resistivity ρ_{xx} at selected pressures up to 44.9 GPa.

IV. MAGNETISM AND ELECTRICAL TRANSPORTS

The temperature and pressure dependences of the magnetization are shown in Fig. 2(a). At 0.1 GPa, the magnetization increases rapidly with decreasing temperature below the Curie temperature $T_C \sim 174$ K, similar to previous results at ambient pressure.[16,17] Here the Curie temperature T_C is obtained from the first-order derivative of the $M-T$ curve. With increasing pressure, both T_C and the magnitude of magnetization decrease monotonically. Figure 2(b) shows the temperature dependence of the resistivity ρ_{xx} of $Co_3Sn_2S_2$ at zero field and selected pressures. At 0.2 GPa, the resistivity exhibits a metallic behavior in the whole temperature range. A sluggish kink appears at ∼167 K, as indicated by the arrow, which is obtained from the first derivative of the $\rho_{xx}-T$ curve. This feature is related to the paramagnetic-ferromagnetic transition in Fig. 2(a). Upon further compression, the metallic behavior maintains to the highest pressure of 44.9 GPa. Meanwhile, the sluggish kink shifts to lower temperatures gradually and becomes almost indistinguishable above 11.6 GPa, in accordance with the gradual suppression of the ferromagnetism as increasing pressure [Fig. 2(a)]. In addition, compression reduces the whole ρ_{xx} greatly and no superconductivity is observed down to 1.8 K and up to 44.9 GPa.

Figures 3(a)-3(g) display hysteresis loops in the Hall measurement under different pressures, which are characteristic of the AHE in $Co_3Sn_2S_2$. Firstly, starting at 0.2 GPa, the saturation value of the Hall resistivity ρ_H first increases upon warming and then decreases; meanwhile, hysteresis loops can be clearly observed up to around T_C. Similar trends are also observed with further increasing pressure to 17.6 GPa, except that the highest saturation value decreases progressively. Secondly, at 20.0 GPa, no evident hysteresis loop is observed through the whole temperature range [Fig. 3(g)], indicating significant suppression of the AHE. Thirdly, the ordinary Hall coefficient at high temperature changes from a positive sign to a negative one when going from 4.9 to 7.1 GPa [Figs. 3(c)-3(d) or Appendix B], which implies a pressure-induced crossover of the charge carrier type from low-pressure hole dominated to high-pressure electron dominated. Finally, the coercive field H_C for all pressures decreases almost linearly with increasing temperature except in the vicinity of T_C [Figs. 3(h)]. Compared with the reported value at ambient pressure (∼0.35 T at 5 K),[16] the H_C at 5 K here is enhanced by two-four times. This enhanced H_C as well as the reduced saturation value of ρ_H may be due to disorder or stress gradient within the sample space as solid NaCl pressure transmitting medium was used in the experiments.

In Fig. 4(a), we plot the temperature variation of the anomalous Hall resistivity ρ_{xy}^A of $Co_3Sn_2S_2$ at various pressures to 17.6 GPa. Upon cooling, the anomalous Hall resistivity at 0.2 GPa increases remarkably around T_C,

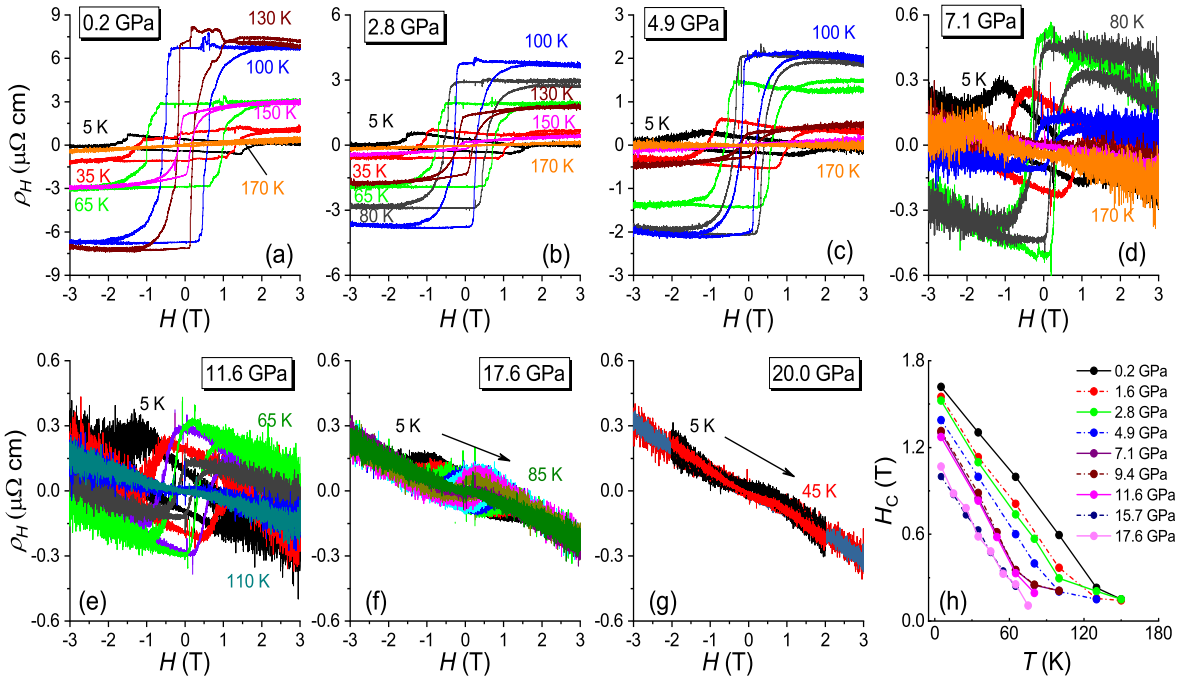

FIG. 3. (a-g) Magnetic field dependence of the Hall resistivity ρ_H at various temperatures and selected pressures. (h) Temperature dependence of the coercive field H_C at different pressures.

and shows a peak value of ~ 8 $\mu\Omega$ cm at $T_{max} \sim 120$ K. As mentioned above, this peak value is smaller than those reported at ambient pressure.[16,17] Below T_{max}, the Hall resistivity decreases monotonically with decreasing temperature. The whole temperature evolution of the anomalous Hall resistivity is in agreement with that at ambient pressure.[16] With further increasing pressure, both the peak value of $-\rho_{xy}^A$ and T_{max} decrease gradually, corresponding to the suppression of the ferromagnetism [Fig. 2(a)]. At 17.6 GPa, the peak value of $-\rho_{xy}^A$ reduces to ~ 0.1 $\mu\Omega$ cm and the $\rho_{xy}^A - T$ curve shows a very broadening shape ranging from 5 to 75 K [inset of Fig. 4(a)].

The temperature dependence of the AHC σ_{xy}^A ($\sigma_{xy}^A = -\rho_{xy}^A/[(\rho_{xy}^A)^2 + (\rho_{xx})^2)]$) is presented in Fig. 4(b). With decreasing temperature, σ_{xy}^A at 0.2 GPa first increases below T_C and then decreases gradually after reaching a maximum of ~ 250 Ω^{-1} cm^{-1}. However, the pressure evolution of σ_{xy}^A at low temperatures is non-monotonic; it first increases from 0.2 to 4.9 GPa and then starts to decrease abruptly upon further compression. Meanwhile, a pressure-induced crossover of the charge carrier type occurs simultaneously [Figs. 3(c)-3(d) or Appendix B]. In addition, we plot the σ_{xy}^A as a function of the longitudinal conductivity σ_{xx} in Fig. 4(c). One can find that σ_{xx} ranges from 10^4 to 10^6 Ω^{-1} cm^{-1} with pressures to 17.6 GPa; roughly, σ_{xy}^A varies slightly with σ_{xx} at low temperatures, suggesting that the present system is in the intermediate regime.[10] Interestingly, the anomalous Hall resistivity $-\rho_{xy}^A$ below T_{max} and at different pressures can be scaled with the longitudinal resistivity ρ_{xx} as a power law of $-\rho_{xy}^A \propto \rho_{xx}^2$ [Fig. 4(d)].

Based on the pressure evolutions of T_C and T_{max}, we construct a temperature-pressure phase diagram for $Co_3Sn_2S_2$ as displayed in Fig. 4(e). When the temperature is above T_C (below T_{max}), the system is of paramagnetic (ferromagnetic) phase; in the intermediate temperature region, a mixture of ferromagnetic and antiferromagnetic phases may appear as proposed by Guguchia *et al.*.[22] On the other hand, it is clear that both T_C and T_{max} decrease linearly upon compression. By linearly extrapolating the trends of T_C vs. P and T_{max} vs. P to higher pressures, one finds that the two curves eventually intersect at a common pressure $P_C \sim 22$ GPa. Around the critical pressure P_C, both the ferromagnetism and the AHE are suppressed simultaneously.

V. THEORETICAL CALCULATIONS AND DISCUSSION

In order to understand the AHE under pressure, we investigated the pressure effect on the band structure, the AHC and the Weyl nodes through first-principle calculations. According to Figs. 5(a)-5(b), we find that compression not only enlarges some local band gap (such as L point) but also shifts the Fermi energy away from the resonant enhancement regions (gapped nodal rings) of the AHC. Meanwhile, our calculations also show that

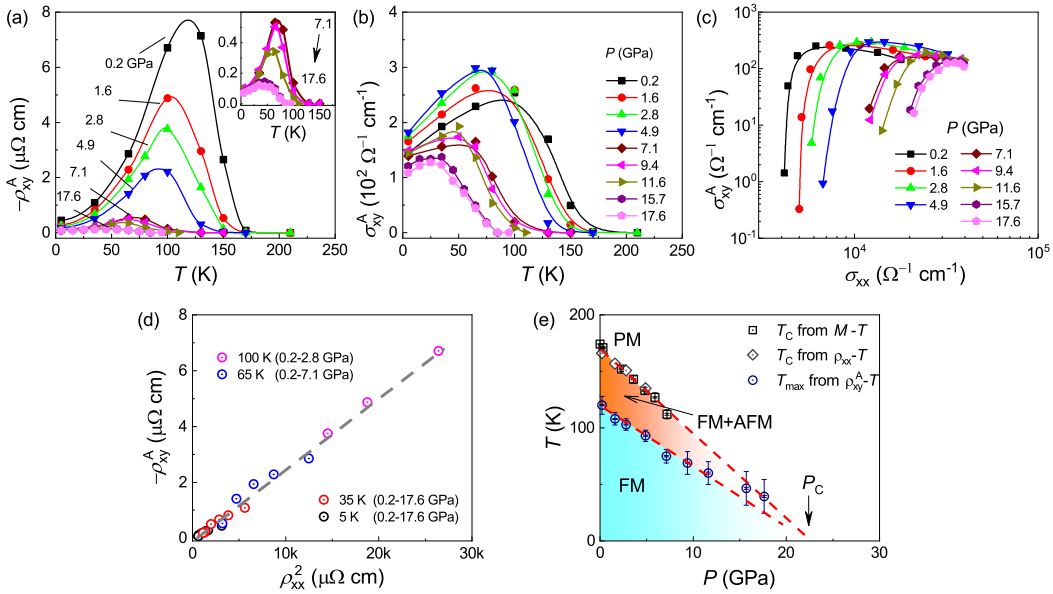

FIG. 4. (a) Temperature dependence of the anomalous Hall resistivity ρ_{xy}^{A} under different pressures. Inset shows an enlarged view of $\rho_{xy}^{A} - T$ from 7.1 to 17.6 GPa. (b) Temperature dependence of the AHC σ_{xy}^{A} under different pressures. (c) Plot of AHC σ_{xy}^{A} as a function of σ_{xx}. (d) Anomalous Hall resistivity ρ_{xy}^{A} as a function of ρ_{xx}^{2}. Only data below T_{max} is taken. (e) Temperature versus pressure phase diagram for $Co_3Sn_2S_2$. PM and FM stand for paramagnetic and ferromagnetic phases, respectively. FM+AFM refers to a mixture of ferromagnetic and antiferromagnetic phases as speculated by Guguchia *et al.* P_C, obtained by linear extrapolations of the low-pressure data, denotes a critical pressure where the ferromagnetism and AHE vanish completely.

the electron pockets around the G point grow up gradually with pressure (see Fig. 8 in Appendix C), in excellent line with our experimental observation of a pressure-induced change of the charge carrier type. In addition, our calculations further reveal that high pressure can effectively tune the Berry curvature of Bloch bands (the evolution of Berry curvature under pressures is given in Fig. 9 in Appendix C and thereby modify the AHC accordingly. It is clear that the intrinsic AHC strongly depends on the doping electron number per unit cell N_e and on the pressure, as shown in Fig. 5(c). When the N_e lies at around 1.03 ($E_F \sim 0.2$ eV), the intrinsic AHC changes non-monotonically with pressure [inset of Fig. 5(c)], qualitatively consistent and quantitatively comparable ($\sim 200\ \Omega^{-1}\ \mathrm{cm}^{-1}$) with the pressure evolution of the AHC observed experimentally [Fig. 4(c)].

A long distance Δ_d between Weyl nodes with opposite chirality in momentum space usually leads to a large intrinsic AHC σ_{xy}^{A}, as is described by $\sigma_{xy}^{A} \propto \Delta_d \cdot e^2/h$.[37] We thus further track the evolution of the Weyl nodes ($\sim$ 0.2 eV). At ambient pressure, the AHC is dominated by the Weyl nodes, marked by red dots Δ_d^{red} in Fig. 5(d). Upon initial compression, Δ_d^{red} becomes a little longer. However, at around 8.46 GPa another two bands touch with each other, leading to a new pair of Weyl nodes with an opposite vector as labeled by blue dots [Figs. 5(e)-5(f)]. With further increasing pressure, the new pair of Weyl nodes moves towards to the original one, making the effective Weyl nodes distance Δ_d^{eff} shortening (Δ_d^{eff}=Δ_d^{red}-Δ_d^{blue}), and eventually the two pairs annihilate with each other (Δ_d^{eff}=0). This could account for the observed non-monotonic change of the AHC [Fig. 3(c)]. The consistency between calculations and experiments suggests that the intrinsic mechanism due to the Berry curvature dominates the AHE at high pressures.

VI. CONCLUSIONS

In summary, we have studied the high pressure effect on the AHE in $Co_3Sn_2S_2$. While the structure of $Co_3Sn_2S_2$ is stable with pressures up to 50.9 GPa, both the anomalous Hall resistivity and ferromagnetism of $Co_3Sn_2S_2$ are gradually suppressed and finally disappears above 22 GPa. The AHC first increases to 4.9 GPa and then begins to decreases abruptly above 7.1 GPa. Meanwhile, a pressure-induced crossover of the charge carrier type from the low-pressure hole-dominated to high-pressure electron-dominated occurs. Our first-principle calculations qualitatively support these experimental observations, suggesting that the intrinsic mechanism should still dominate the AHE of $Co_3Sn_2S_2$ under high pressure.

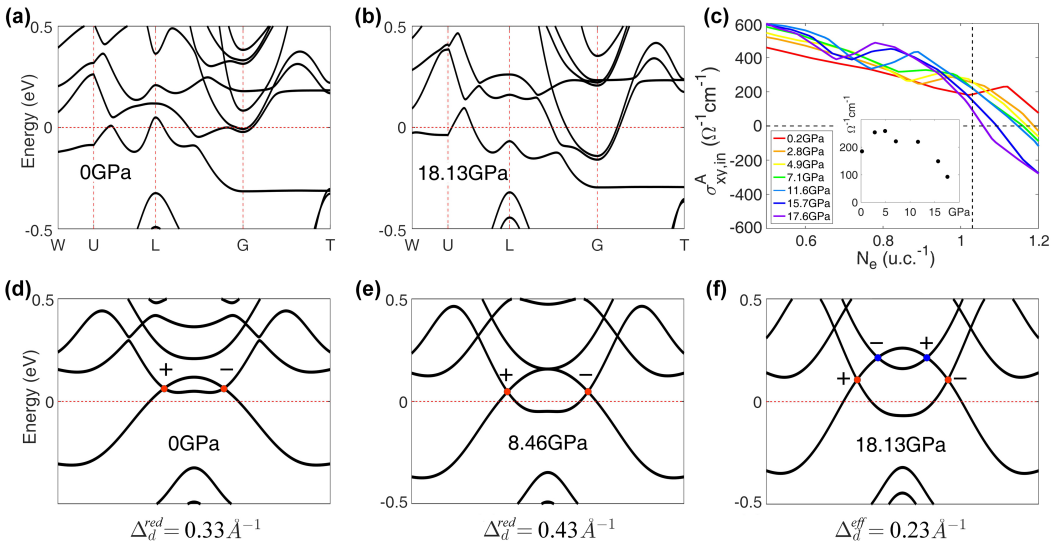

FIG. 5. (a-b) Electronic band structures at zero pressure and a high pressure of 18.13 GPa. (c) Doping electron number per unit cell (N_e) dependent intrinsic AHC at selected pressures, where N_e=0 refers to the case without doping (E_F=0). Insert in (c) plots the pressure dependent AHC at N_e=1.03 (vertical dashed line in the main figure). (d-f) Evolution of Weyl nodes labeled by red and blue dots near the Fermi level at selected pressures, where Δ_d^{red} (Δ_d^{blue}) represents the length of the vector connecting the red (blue) Weyl nodes and Δ_d^{eff}=Δ_d^{red}-Δ_d^{blue} means the effective Weyl nodes distance. ± refers to the chirality of each Weyl point.

ACKNOWLEDGMENTS

This work was supported by the National Key R&D Program of the MOST of China (Grants No. 2018YFA0305700, No. 2016YFA0401804, No. 2016YFA0300600), the NSFC (Grants No. U1632275, No. 11574323, No. 11874362, No. 11804344, No. 11804341, No. 11704387, No. 11605276, No. U1832209, No. 11734003), the NSF of Anhui Province (Grants No. 1708085QA19, No. 1808085MA06, No. 1908085QA18), the Users with Excellence Project of Hefei Science Center CAS (Grant No. 2018HSC-UE012), the Major Program of Development Foundation of Hefei Center for Physical Science and Technology (Grant No. 2018ZYFX002), the Strategic Priority Research Program of Chinese Academy of Sciences (Grant No. XDB30000000) and the 100 Talents Program of Chinese Academy of Sciences (CAS). H.D.Z. thanks the support from NSF-DMR-1350002. The x-ray work was performed at the Beamline BL15U1, SSRF, Shanghai.

* These authors contributed equally to this work.
† jhzhou@hmfl.ac.cn
‡ ygyao@bit.edu.cn
§ zryang@issp.ac.cn

[1] N. P. Armitage, E. J. Mele, and A. Vishwanath, Weyl and Dirac semimetals in three-dimensional solids. Rev. Mod. Phys. **90**, 015001 (2018)
[2] H. Weng, X. Dai, and Z. Fang, Topological semimetals predicted from first-principles calculations. J. Phys.: Condens. Matter **28**, 303001 (2016).
[3] B. Yan and C. Felser, Topological Materials: Weyl Semimetals. Annu. Rev. Condens. Matter Phys. **8**, 337 (2017).
[4] M. Z. Hasan, S. Y. Xu, I. Belopolski, and S. M. Huang, Discovery of Weyl fermion semimetals and topological Fermi arc states. Annu. Rev. Condens. Matter Phys. **8**, 289 (2017).
[5] C. Zhang, H.-Z. Lu, S.-Q. Shen, Y. P. Chen, and F. Xiu, Towards the manipulation of topological states of matter: a perspective from electron transport. Sci. Bull. **63**, 580 (2018).
[6] T. Zhang, Y. Jiang, Z. Song, H. Huang, Y. He, Z. Fang, H. Weng, and C. Fang, Catalogue of topological electronic materials. Nature **566**, 475 (2019).
[7] F. Tang, H. C. Po, A. Vishwanath, and X. G. Wan, Comprehensive search for topological materials using symmetry indicators. Nature **566**, 486 (2019).
[8] M. G. Vergniory, L. Elcoro, C. Felser, N. Regnault, B. Andrei Bernevig, and Z. J. Wang, A complete catalogue of high-quality topological materials. Nature **566**, 480 (2019).
[9] D. Xiao, M. C. Chang, and Q. Niu, Berry phase effects on electronic properties. Rev. Mod. Phys. **82**, 1959 (2010).
[10] N. Nagaosa, J. Sinova, S. Onoda, A. H. MacDonald, and N. P. Ong, Anomalous Hall effect. Rev. Mod. Phys. **82**, 1539 (2010).
[11] N. A. Sinitsyn, Semiclassical theories of the anomalous Hall effect. J. Phys.: Condens. Matter **20**, 023201 (2008).

[12] Z. Fang, N. Nagaosa, K. S. Takahashi, A. Asamitsu, R. Mathieu, T. Ogasawara, H. Yamada, M. Kawasaki, Y. Tokura, and K. Terakura, The anomalous Hall effect and magnetic monopoles in momentum space. Science **302**, 92 (2003).
[13] Y. G. Yao, L. Kleinman, A. H. MacDonald, J. Sinova, T. Jungwirth, D.-s. Wang, E. G. Wang, and Q. Niu, First principles calculation of anomalous Hall conductivity in ferromagnetic bcc Fe. Phys. Rev. Lett. **92**, 037204 (2004).
[14] C. M. Hurd, *The Hall Effect in Metals and Alloys*. (Cambridge University Press, 1972).
[15] C. L. Chien and C. R. Westgate, *The Hall Effect and Its Applications*. (Plenum Press, New York, 1980).
[16] E. K. Liu, Y. Sun, N. Kumar, L. Muechler, A. Sun, L. Jiao, S.-Y. Yang, D. F. Liu, A. Liang, Q. Xu, J. Kroder, V. Sub, H. Borrmann, C. Shekhar, Z. Wang, C. Xi, W. Wang, W. Schnelle, S. Wirth, Y. Chen, S. T. B. Goennenwein, and C. Felser. Giant anomalous Hall effect in a ferromagnetic kagome-lattice semimetal. Nat. Phys. **14**, 1125 (2018).
[17] Q. Wang, Y. F. Xu, R. Lou, Z. H. Liu, M. Li, Y. B. Huang, D. W. Shen, H. M. Weng, S. C. Wang, and H. C. Lei, Large intrinsic anomalous Hall effect in half-metallic ferromagnet $Co_3Sn_2S_2$ with magnetic Weyl fermions. Nat. Commun. **9**, 3681 (2018).
[18] P. Vaqueiro and G. G. Sobany, A powder neutron diffraction study of the metallic ferromagnet $Co_3Sn_2S_2$. Solid State Science **11**, 513 (2009).
[19] W. Schnelle, A. Leithe-Jasper, H. Rosner, F. M. Schappacher, R. Pottgen, F. Pielnhofer, and R. Weihrich, Ferromagnetic ordering and half-metallic state of $Sn_2Co_3S_2$ with the shandite-type structure. Phys. Rev. B **88**, 144404 (2013).
[20] M. A. Kassem, Y. Tabata, T. Waki, and H. Nakamura, Low-field anomalous magnetic phase in the kagome-lattice shandite $Co_3Sn_2S_2$. Phys. Rev. B **96**, 014429 (2017).
[21] K. Geishendorf, R. Schlitz, P. Vir, C. Shekhar, C. Felser, K. Nielsch, S. T. B. Goennenwein, and A. Thomas, Magnetoresistance and anomalous Hall effect in micro-ribbons of the magnetic Weyl semimetal $Co_3Sn_2S_2$. Appl. Phys. Lett. **114**, 092403 (2019).
[22] Z. Guguchia, J. Verezhak, D. Gawryluk, S. S. Tsirkin, J.-X. Yin, I. Belopolski, H. Zhou, G. Simutis, S.-S. Zhang, T. A. Cochran, G. Chang, E. Pomjakushina, L. Keller, Z. Skrzeczkowska, Q. Wang, H. C. Lei, R. Khasanov, A. Amato, S. Jia, T. Neupert, H. Luetkens, and M. Z. Hasan, Tunable berry curvature through magnetic phase competition in a topological kagome magnet. *Preprint at arXiv: 1904.09353v1.*
[23] Q. Xu, E. Liu, W. Shi, L. Muechler, J. Gayles, C. Felser, and Y. Sun, Topological surface Fermi arcs in the magnetic Weyl semimetal $Co_3Sn_2S_2$. Phys. Rev. B **97**, 235416 (2018).
[24] Shama, R. K. Gopal, and Y. Singh, Observation of planar Hall effect in the magnetic Weyl semimetal $Co_3Sn_2S_2$. *Preprint at arXiv: 1810.04867v1.*
[25] S. N. Guin, P. Vir, Y. Zhang, N. Kumar, S. J. Watzman, C. Fu, E. Liu, K. Manna, W. Schnelle, J. Gooth, C. Shekhar, Y. Sun, and C. Felser, Zero-field nernst effect in a ferromagnetic kagome-lattice Weyl-semimetal $Co_3Sn_2S_2$. Adv. Mat., 1806622 (2019).
[26] H. Yang, W. You, J. Huang, C. Xi, C. Cao, M. Tian, Z.-A. Xu, J. Dai, and Y. Li, Giant anomalous Nernst effect in the magnetic Weyl semimetal $Co_3Sn_2S_2$. *Preprint at arXiv: 1811.03485v1.*
[27] M. Csontos, T. Wojtowicz, X. Liu, M. Dobrowolska, B. Janko, J. K. Furdyna, and G. Mihaly, Magnetic Scattering of Spin Polarized Carriers in (In,Mn)Sb Dilute Magnetic Semiconductor. Phys. Rev. Lett. **95**, 227203 (2005).
[28] G. Mihaly, M. Csontos, S. Bordacs, I. Kezsmarki, T. Wojtowicz, X. Liu, B. Janko, and J. K. Furdyna, Anomalous Hall Effect in the (In,Mn)Sb Dilute Magnetic Semiconductor. Phys. Rev. Lett. **100**, 107201 (2008).
[29] M. Csontos, G. Mihaly, B. Janko, T. Wojtowicz, X. Liu, and J. K. Furdyna, Pressure-induced ferromagnetism in (In,Mn)Sb dilute magnetic semiconductor. Nature Materials **4**, 447 (2005).
[30] Minhyea Lee, W. Kang, Y. Onose, Y. Tokura, and N. P. Ong, Unusual Hall Effect Anomaly in MnSi under Pressure. Phys. Rev. Lett. 102, 186601 (2009).
[31] G. Kresse and J. Furthmuller, Efficient iterative schemes for *ab initio* total-energy calculations using a plane-wave basis set. Phys. Rev. B **54**, 11169 (1996).
[32] J. P. Perdew, K. Burke, and M. Ernzerhof, Generalized Gradient Approximation Made Simple. Phys. Rev. Lett. **77**, 3865 (1996).
[33] G. Kresse and D. Joubert, From ultrasoft pseudopotentials to the projector augmented-wave method. Phys. Rev. B **59**, 1758 (1999).
[34] X. Wang, J. R. Yates, I. Souza, and David Vanderbilt, *Ab initio* calculation of the anomalous Hall conductivity by Wannier interpolation. Phys. Rev. B **74**, 195118 (2006).
[35] A. A. Mostofi, J. R. Yates, Y.-S. Lee, I. Souza, D. Vanderbilt, and N. Marzari, wannier90: A tool for obtaining maximally-localised Wannier functions. Comput. Phys. Commun. **178**, 685 (2008).
[36] F. Birch, Phys. Rev. **71**, 809 (1947).
[37] A. A. Burkov, Anomalous Hall effect in Weyl metals. Phys. Rev. Lett. **113**, 187202 (2014).

Appendix A: BASIC CHARACTERIZATION AT AMBIENT/ZERO PRESSURE

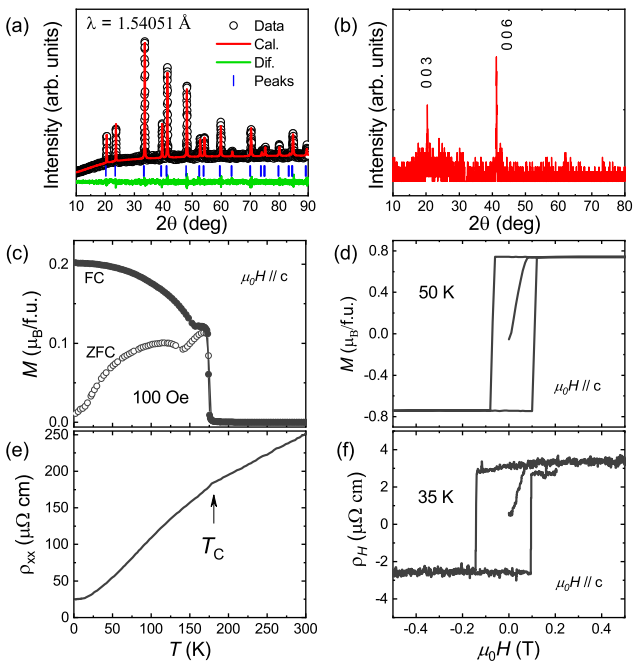

FIG. 6. (a) Powdered and (b) single crystal XRD at room temperature. Le Bail method was used to fit the powdered XRD pattern with the RIETICA program. The refinement results are a=5.370703 Å, c=13.183318 Å, V=329.32 Å^3, R_{wp}=0.0620, R_p=0.0548 and χ^2 = 16.47. (c) Temperature dependence of magnetization for single crystal $Co_3Sn_2S_2$ under field-cooled (FC) and zero-field-cooled (ZFC) sequences at c-axis magnetic field of 100 Oe. (d) Magnetic field dependence of magnetization M at 50 K with the field parallel to c axis. (e) Longitudinal resistivity ρ_{xx} versus T. The arrow indicates a kink at the Curie temperature T_C corresponding to a paramagnetic-to-ferromagnetic transition. (f) Hall resistivity ρ_H versus $\mu_0 H$ measured at 35 K with the field parallel to c axis.

Appendix B: HIGH TEMPERATURE AND HIHG PRESSURE HALL COEFFICIENTS

The initial positive slope of the ordinary Hall signal decreases with pressure and changes into negative at 7.1 GPa with a small absolute value. Though the highest temperature for $p > 7.1$ GPa is not so consistent due to limited machine time, one can still see that the slope of the ordinary Hall signals keeps always negative throughout the temperature widow we measured (Fig. 3). Thus, high pressure could induce a crossover of charge carrier type from the low-pressure hole dominated to high-pressure electron dominated.

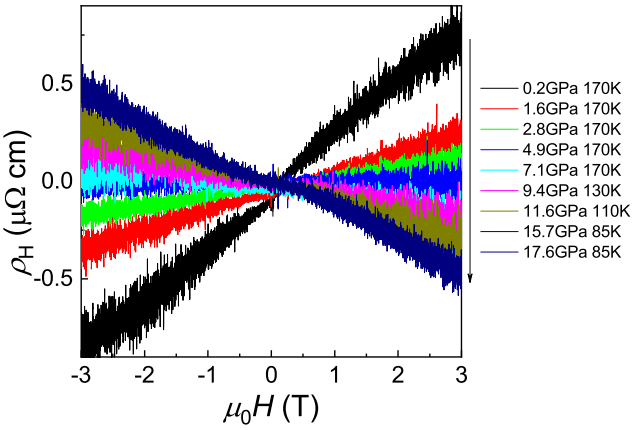

FIG. 7. Magnetic field dependence of the ordinary Hall resistivity near or above T_C.

Appendix C: CALCULATED DETAILED BAND STRUCTURES AND DISTRIBUTIONS OF THE BERRY CURVATURE AT HIGH PRESSURES

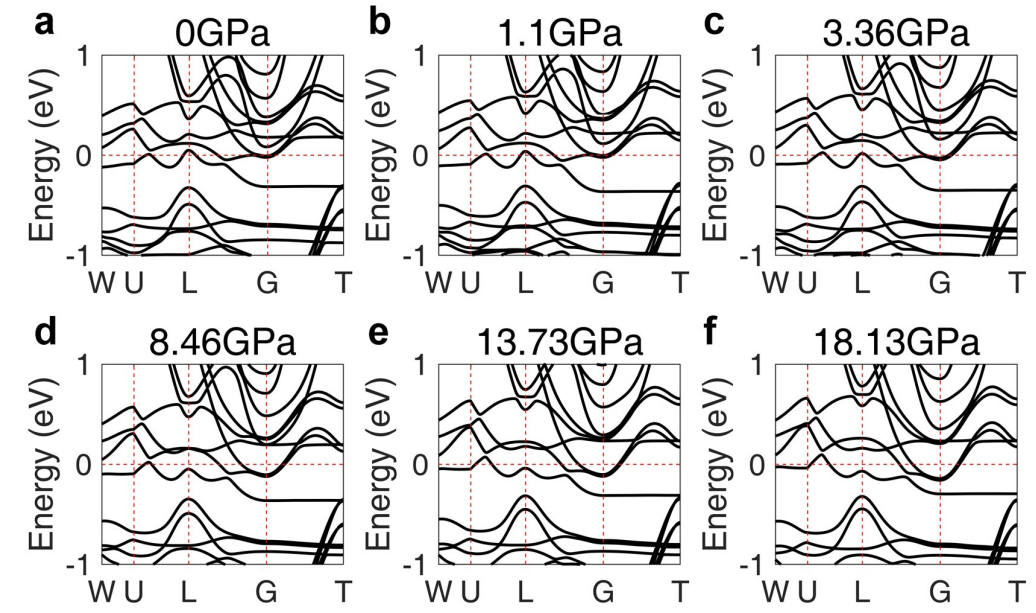

FIG. 8. Band structures of $Co_3Sn_2S_2$ along the W-U-L-G-T path at various pressures obtained from first-principle calculations.

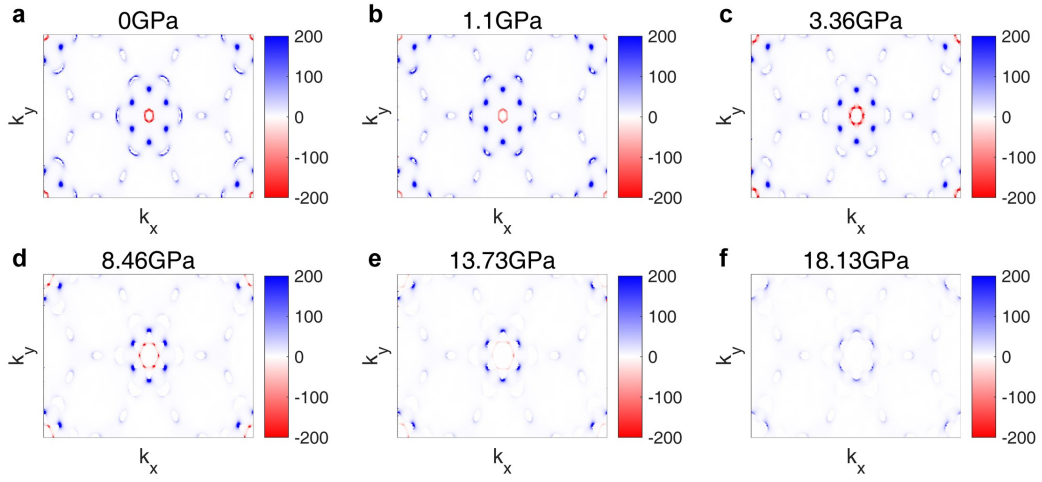

FIG. 9. Distributions of the Berry curvature $\Omega_{xy}(k)$ at the k_x-k_y plane (k_z=0) in the Brillouin zone for $Co_3Sn_2S_2$ at various pressures.